Chapter 3

Reduced Graphene Oxide Supported MoNi$_4$/MoO$_2$ Nanorods for Hydrogen Evolution Reaction

3.1 Introduction

In this chapter, we present the development of $MoNi_4/MoO_2$:rGO nanocomposites and their structural characterizations, such as (XRD, Raman, FESEM, and TEM/HRTEM) followed by application for hydrogen evolution reaction (HER). Over the past few years, several nonprecious materials have been exploited for HER via water splitting, including, transition metal di-chalcogenides (TMDs) [1-4], borides [5, 6], nitrides [7], carbides [8], phosphides [9], metal alloys and intermetallics [10-12], oxides [13], plasmonic nanoparticles [14, 15], and heteroatom-doped carbon nanostructures [16, 17], and several others. Among them, metal alloys and carbon allotropes (such as CNTs, graphene, rGO) draw increasing research interest due to their tuned electronic structure, high electrical conductivity, accelerated charge transfer kinetics, faster hydrogen adsorption/desorption, smaller diffusion coefficient, remarkable mechanical properties, and outstanding aqueous stability [10, 11, 18, 19].

Recently, Mo-Ni based intermetallics (Mo_xNi_y) have been proposed as promising candidates for the HER electrocatalysts owing to their alloying, where Mo atoms shows superior adsorption properties towards hydrogen, while Ni atoms act as an excellent water dissociation centers [11, 20, 21]. Therefore, Ni–Mo-based alloy electrocatalysts (Mo_xNi_y) can be promising candidates to speed up the sluggish HER kinetics under alkaline medium and effectively reduce the Volmer-step energy barrier. Zhou et al. demonstrates that Mo-Ni alloy-based hollow structure (MoNi-HS) exhibits excellent HER activity in alkaline solution [22]. Lihua An et al. reported graphene embedded $MoNi_4$-$NiMoO_4$ nanorods for overall water splitting in a 1M KOH solution [19]. Chen et al. synthesized $MoNi_4/MoO_{3-x}$ nanorods for HER application where the dual activity of $MoNi_4$ nanocrystal embedded on MoO_{3-x} boosts the overall catalytic activity [10]. Zhang et al. reported $MoNi_4$ alloys covered by MoO_2 nanosheets on Ni foam exhibiting high HER performance due to their exposed active sites, high specific surface area, and high conductivity [11]. Similarly, Singh et al., showed that

$MoNi_4/MoO_2$ nanorods can be simultaneously used as catalysts as well as the conducting pathways for a TMDs-based hybrid structure [18]. These reports further suggest that the highly efficient Mo_xNi_y alloys could have the potential for anticipated applications in HER via water dissociation reactions.

Furthermore, graphene is a two-dimensional planer sheet of sp^2 bonded monoatomic carbon layer, which was packed into a sp^2 bonded honeycomb crystal lattice. Since its invention, graphene has been widely used as a supercapacitors [23], batteries [24], solar cells [25], catalysis/electrocatalysis [26], optoelectronics devices [27], photocatalysis [28], and good support material [29, 30], for graphene-based high-capacity composites due to its unique properties such as ultrahigh specific surface area, excellent mechanical flexibility, superior electrical conductivity, and high chemical and thermal stability [31, 32]. In particular, the extremely high electron mobility is expected to be beneficial for electrode material for overall water splitting via the electrochemical process [33]. Graphene, graphene oxide (GO), and reduced graphene oxides (rGO) have been widely proposed as potential non-noble materials to replace Pt owing to their extraordinary electrical conductivity and electron mobility, rapid charge transfer kinetics, inert basal plane, and faster Heyrovsky steps that could even accelerate the rate of water splitting [33-37]. Among other graphitic allotropes, reduced graphene oxide (rGO) exhibits more favorable electrocatalytic performances because of its enhanced surface defects [38], surface-bound functional molecules [39, 40], localized electron concentrations [41], and improved hydrophilicity while having high electrical conductivity [41-43].

In this chapter, we report the synthesis of $MoNi_4/MoO_2$ nanorods, reduced graphene oxide (rGO) sheets and MoNi4/MoO2:rGO nanocomposites and demonstrate the electrocatalytic activity for HER via electrochemical water splitting (EWS). Reduced graphene oxide (rGO) was synthesized using the modified hummers' method followed by the heat-treatment and

used as the nucleation point on which $MoNi_4/MoO_2$ forms in the hydrothermal method. The nanocomposites were characterized using XRD, SEM, TEM/HRTEM, and Raman spectroscopy in order to check the structure, morphology, and bonding properties followed by electrochemical testing for investigating the electrocatalytic activity of the nanocomposite for HER via water splitting.

3.2. Results and discussions

The $MoNi_4/MoO_2$:rGO nanocomposite is synthesized by using the hydrothermal method and the entire processes were described in detail in chapter 2 (sections 2.1.2 to 2.1.5). The phase and crystal structure of as-synthesized $MoNi_4/MoO_2$:rGO nanocomposite were investigated by the X-ray diffraction (XRD) technique. Figure 3.1a shows the nanocomposite's X-ray diffraction pattern (XRD) of $MoNi_4/MoO_2$:rGO (green curve). Diffraction peaks located at 2θ = 36.72°, 53.20°, and 66.12° correspond to (11-2), (121), and (202) crystal planes of metallic MoO_2 nanorods (JCPDS No. 98-001-7724), while the presence of XRD diffraction patterns observed at 2θ = 26.08° and 44.26° correspond to the (002) and (100) crystal plans of reduced graphene oxide (rGO) (JCPDS No.01-0640). A few XRD peaks are obtained at 2θ = 44.26°, 51.58°, and 66.12° corresponding to the (121), (002), and (512) crystal planes of $MoNi_4$ (JCPDS No. 98-007-4658). There are no other impurity peaks observed in the XRD data of the nanocomposite, which further confirms the presence of $MoNi_4/MoO_2$ and rGO in the as-synthesized nanocomposite.

Figure 3.1b shows the Raman spectrum of rGO, $MoNi_4/MoO_2$, and $MoNi_4/MoO_2$:rGO nanocomposite, the D and G band vibration mode of graphene can be observed from 1300 to 1600 cm^{-1}. In $MoNi_4/MoO_2$:rGO nanocomposite, two Raman modes were observed at 1340 and 1560 cm^{-1}, which corresponds to the D and G band of graphene sheets. The D band G band is associated with the in-plane starching vibration of the pairs of C sp^2 atoms (E_{2g}

phonons) and the breathing modes of rings or K-point phonons of the A_{1g} symmetry. Apart from graphene characteristics peaks, Raman modes were observed at 339, 811, 883, and 936 cm^{-1}, respectively, which are corresponding Mo-O-Mo and Mo=O stretching modes of MoO_2, further conforming to the successful synthesis of $MoNi_4/MoO_2$:rGO nanocomposite.

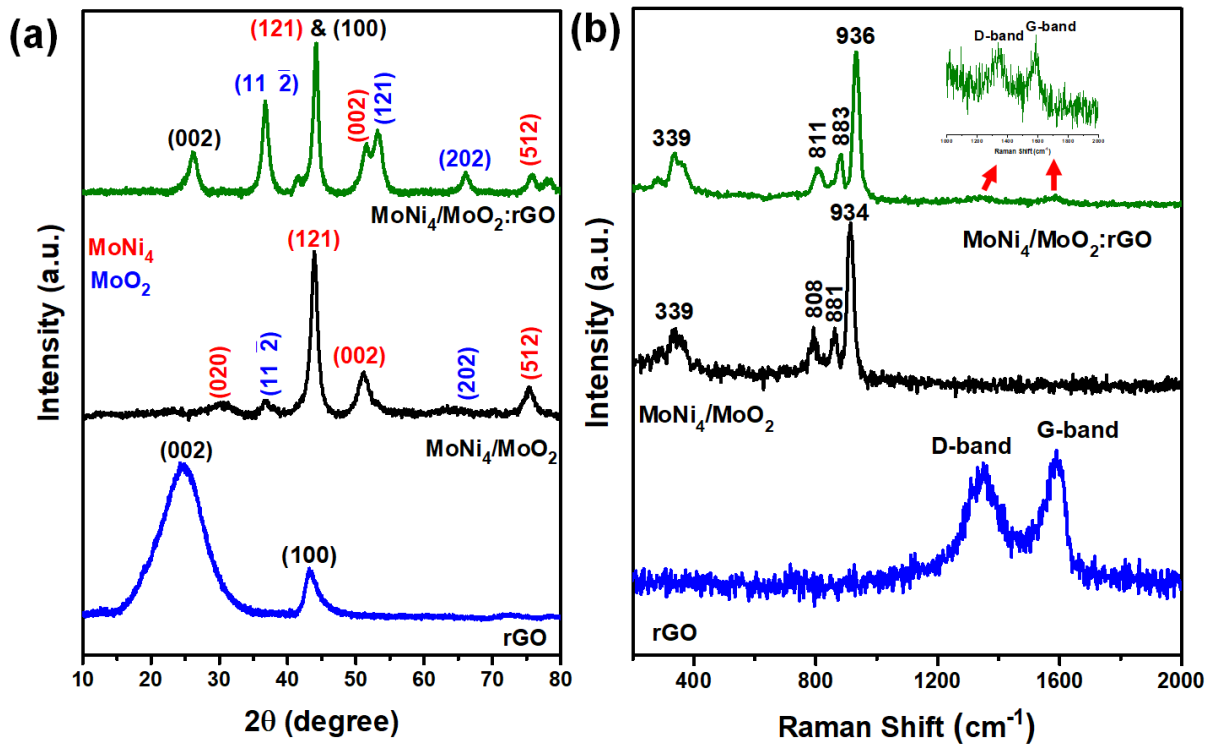**Figure 3.1:** Shows *(a) X-ray diffraction (XRD) pattern; (b) Raman spectra of rGO, MoNi₄/MoO₂, and MoNi₄/MoO₂:rGO nanocomposite.*

Scanning electron microscopy (SEM) was employed to investigate the morphology of as-synthesized $MoNi_4/MoO_2$ nanorod and $MoNi_4/MoO_2$:rGO nanocomposite. We have characterized as-synthesized $MoNi_4/MoO_2$ nanorods as shown in Figure 3.2a and Figure 3.2b, which indicate the MoO_2 nanorods of length of ~3-5 µm. It is also observed that $MoNi_4$ nanocrystals form on the surface of the MoO_2 nanorods, as depicted in Figure 3.2b. The size of the $MoNi_4$ nanocrystals is around 30-50 nm, homogeneously dispersed throughout the surface of the MoO_2 nanorods. Figure 3.2c and Figure 3.2d show the $MoNi_4/MoO_2$:rGO nanocomposite reveals that $MoNi_4/MoO_2$ nanorods are supported by the reduced graphene

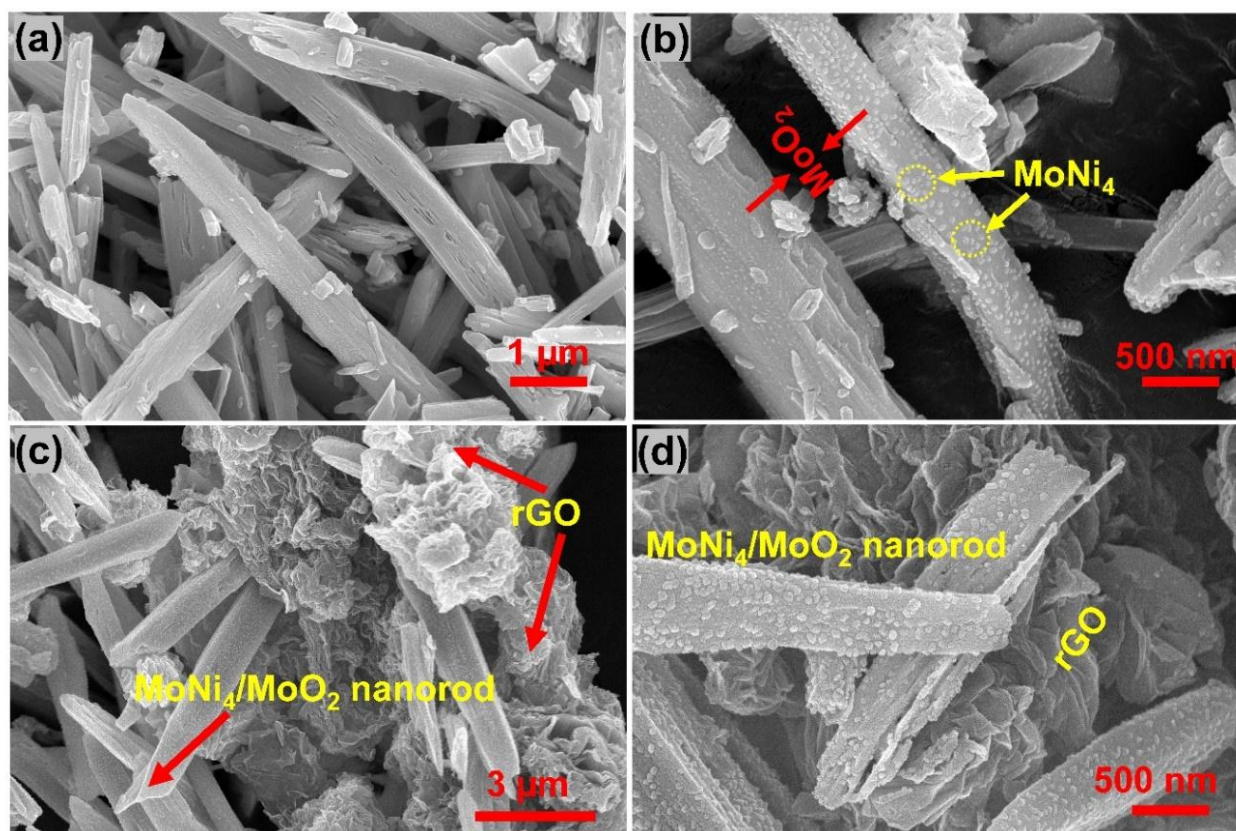oxide (rGO) sheets. Thus, these MoNi$_4$/MoO$_2$ supported with rGO sheets exhibit a significantly high surface area.

Figure 3.2: *Shows the FESEM images of (a) MoNi$_4$/MoO$_2$ nanorods; (b) MoNi$_4$ nanocrystals grown on MoO$_2$ nanorods; (c and d) MoNi$_4$/MoO$_2$:rGO nanocomposites where MoNi$_4$ nanocrystals grown on MoO$_2$ nanorods were supported with the rGO sheets.*

Figure 3.3 shows the transmission electron micrograph (TEM)/high-resolution transmission electron micrographs (HRTEM) of the as-synthesized MoNi$_4$/MoO$_2$ nanorods. The TEM images of MoNi$_4$/MoO$_2$ nanorods are shown in Figure 3.3a and Figure 3.3b, which illustrate that black dots of MoNi$_4$ nanocrystals are well-dispersed on the matrix of MoO$_2$ nanorods. These dispersed nanosized MoNi$_4$ activate the nanostructure for the improved electrocatalytic reactions. Figure 3.3c shows the HETEM of nanorods with lattice fringes with lattice distances of 0.16 nm and 0.35 nm correspond to the (031) plane of MoNi$_4$ and the (110) plane

of MoO$_2$, respectively. The selected area electron diffraction pattern (SAED) shows diffraction patterns of the (121), (031) crystal planes of MoNi$_4$ and the (112), (024) lattice planes of MoO$_2$ as shown in Figure 3.3d.
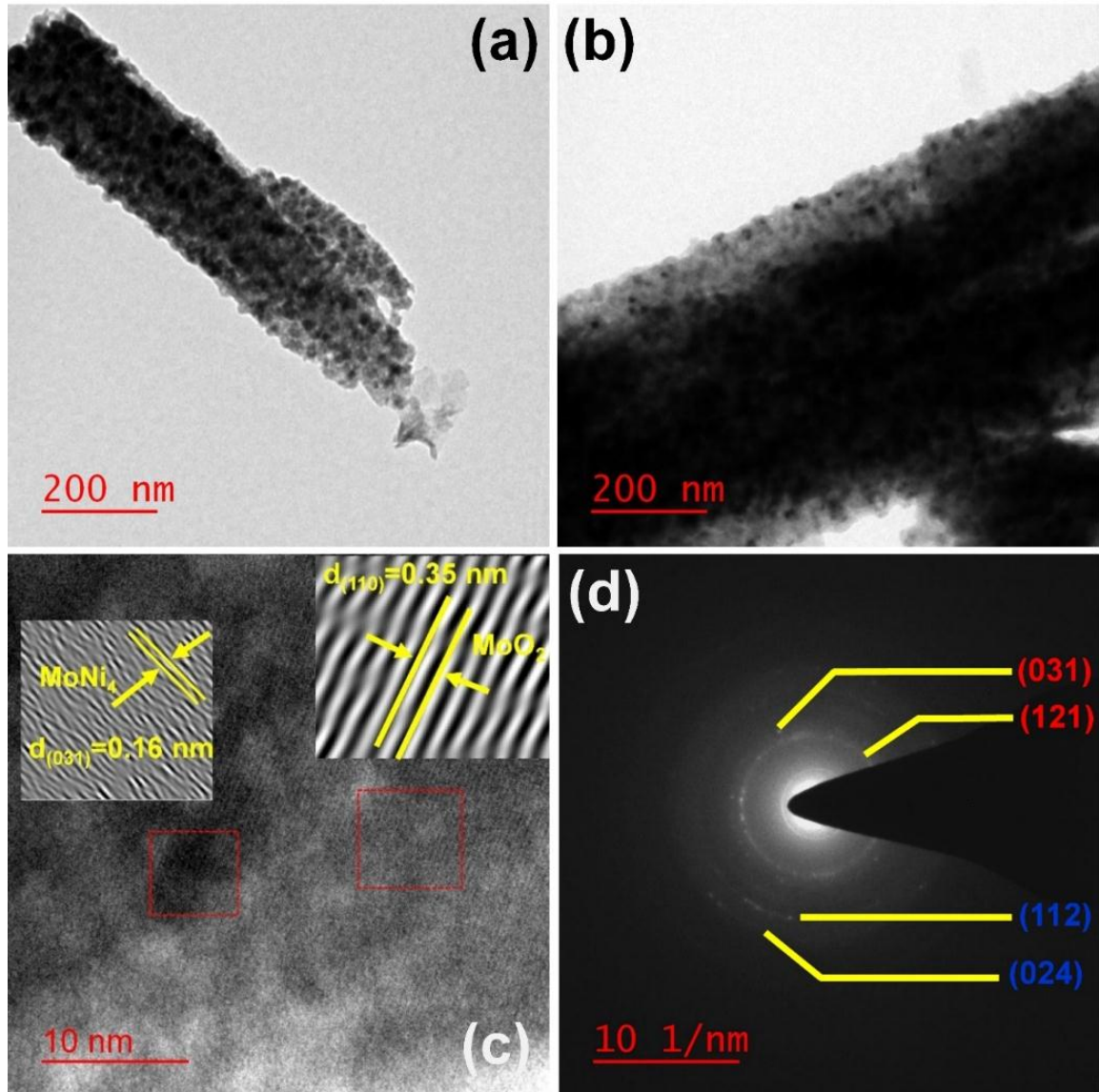

Figure 3.3: *Shows the transmission electron micrographs (TEM) of (a and b) MoNi$_4$/MoO$_2$ nanorods where MoNi$_4$ nanocrystals are grown on MoO$_2$ nanorods (black dots); (c) high-resolution transmission electron micrographs (HRTEM) and (d) SAED pattern of MoNi$_4$/MoO$_2$.*
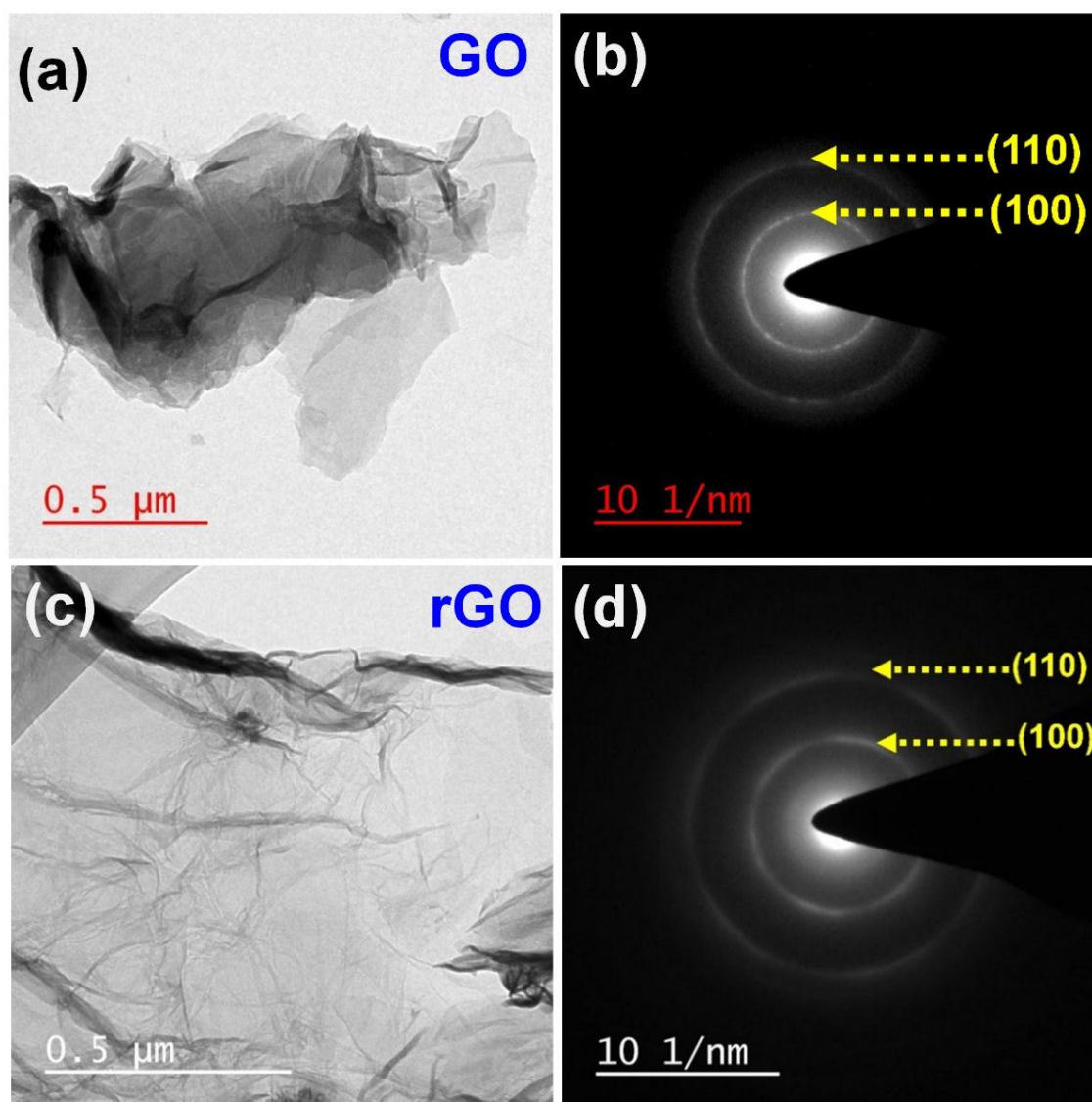
Figure 3.4: *Illustrates (a) Transmission electron micrograph and (b) SAED pattern of graphene oxide (GO); (c) Transmission electron micrograph (TEM) and (d) SAED of reduced graphene oxide (rGO).*

Figure 3.4 shows the transmission electron micrographs of the as-synthesized graphene oxide (GO) and reduced graphene oxide (rGO) sheets along with their SAED pattern. Figure 3.4a represents the morphology of GO sheets along with SAED data. It is clearly observed that as-prepared GO samples are comparatively thick as it consists of a few graphene layers stacked to each other. The SAED of GO shows the (110) and (100) characteristic planes of sp^2 bonded graphitic crystal. The morphology of as-synthesized rGO shows the stacked layers

are separated out and forms crumpled single-layered structure as (Figure 3.4b), and it also shows that the single layer rGO exhibits large flake size of ~ 5-10 μm.
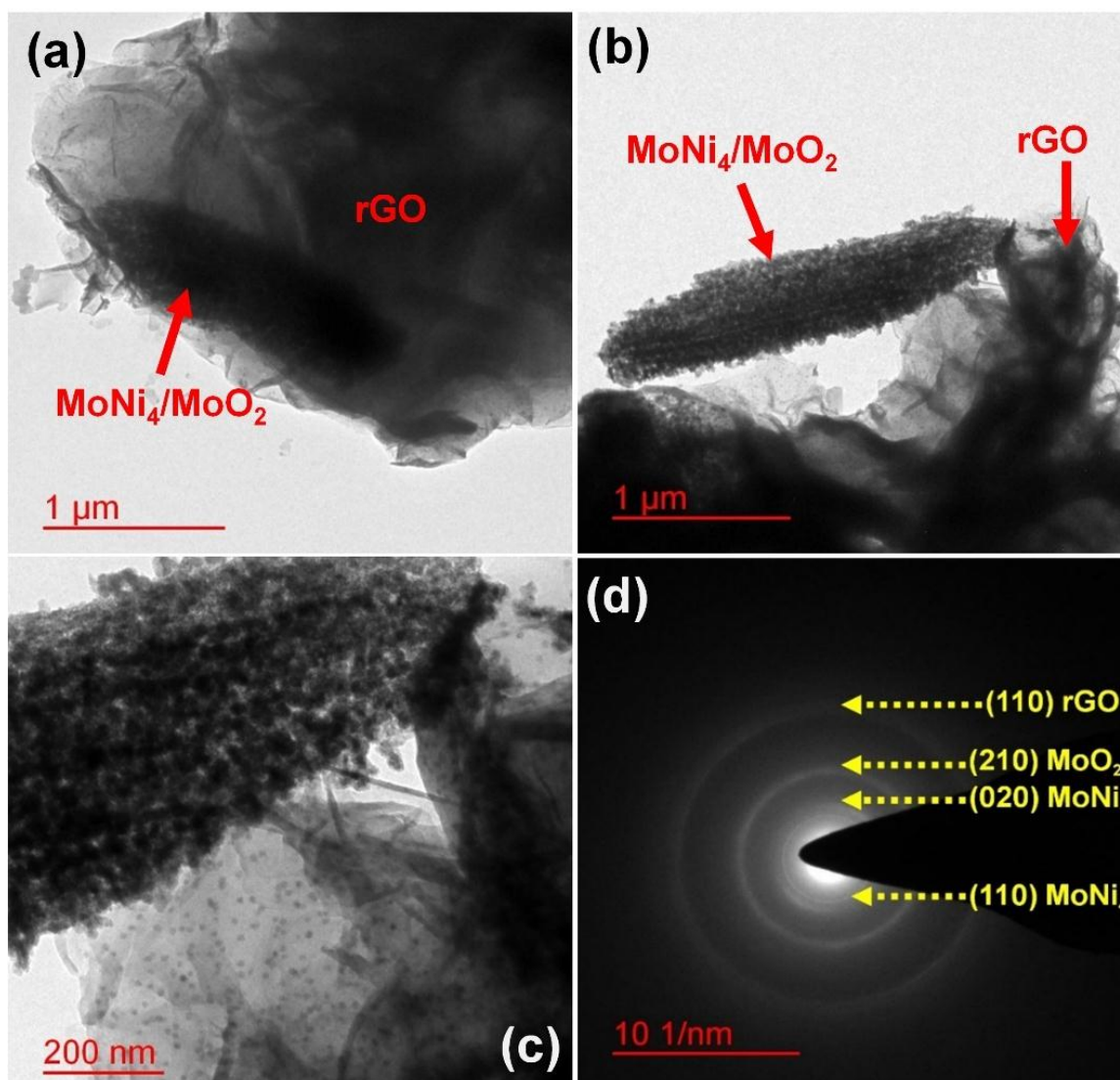

Figure 3.5: Shows the transmission electron micrographs (TEM) of (a, b and c) MoNi$_4$/MoO$_2$:rGO nanocomposite where MoNi$_4$ nanocrystals are grown on MoO$_2$ nanorods are supported by rGO sheets (d) SAED pattern of MoNi$_4$/MoO$_2$:rGO nanocomposite.

Figure 3.5 shows the transmission electron micrograph (TEM) of the as-synthesized MoNi$_4$/MoO$_2$:rGO nanocomposites. MoNi$_4$/MoO$_2$ nanorods were supported with the rGO sheets as shown in Figure 3.5 (a-c). It can be seen from the TEM images that the MoNi$_4$/MoO$_2$ nanorods are entangled with flaky rGO sheets and in a few places, there are

some junction/interface formations occurred between $MoNi_4/MoO_2$ nanorod and rGO. Therefore, our as-synthesized $MoNi_4/MoO_2$:rGO nanocomposite showed a hierarchical nanostructures, where rGO sheets provided a conducting channel to the $MoNi_4/MoO_2$ nanorods to accelerate the charge transfer and reaction rate, thereby improving the performance of electrocatalytic HER. It can also be assumed that the graphene edge-planes are also play significant role in the process of charge transfer, thus, enhancing the electrocatalytic activity as well as the structural stability of those electrodes. The selected area electron diffraction pattern (SAED) shows diffraction patterns of the (110), (021) facet of $MoNi_4$, (210) facet of MoO_2, and (110) facet of rGO, respectively, as shown in Figure 3.5d. Overall, the SEM morphology, TEM/SAED associated with XRD further suggest the formation of an unique nanostructure consists of $MoNi_4/MoO_2$ nanorod embedded with rGO sheets nanocomposites, which we use as electrocatalytic electrodes as discussed in the next part of this chapter.
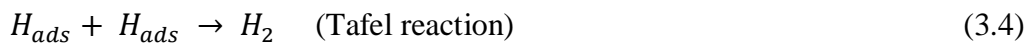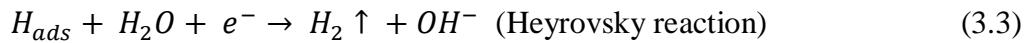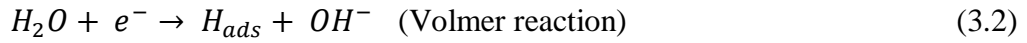
For electrochemical characterizations, we have prepared the electrocatalytic electrodes by drop-casting the ink as-prepared using the as-synthesized powder on nickel foam, which we used as working electrodes for all the samples. The ink was prepared by dispersing the known amount of $MoNi_4/MoO_2$:rGO powder in isopropanol stabilized with Nafion (5 wt. %) solution on Ni foam with the effective area of 1 cm^2 as discussed in chapter 2 (section 2.3.1). In detail, dispersion was done by adding 3 mg of the catalyst power (i.e., $MoNi_4/MoO_2$:rGO) in a 1030 µL solution prepared by adding 30 µL 5% Nafion, 750 µL DI water, 250 µL isopropanol and sonicated for 60 min. to form a homogeneous ink. 1030 µL dispersion is drop-cast on Ni foam in multiple steps of 20 µL followed by drying in ambient conditions. Electrochemical characterizations were performed as discussed in detail in chapter 2 (section 2.3.2), where all the experimental parameters are discussed elaborately. HER activity of the as-synthesized catalysts was investigated in 1M KOH solution by a three-electrode setup

where a graphite rod, Ag/AgCl (saturated with KCl), and as-synthesized catalysts were coated on Ni foam (1×1 cm^2) were used as the counter, reference and working electrode, respectively. In the linear sweep voltammetry (LSV) curve, the η_{10} (as potential at which a current density of 10 mA/cm^2 is achieved) is a critical parameter for assessing the electrocatalytic ability of an electrocatalyst. In general, the small η_{10} value indicated the superior electrocatalyst activity of the electrocatalysts for HER. Figure 3.6a shows the LSV curve of MoNi$_4$/MoO$_2$ nanorod, rGO, and MoNi$_4$/MoO$_2$:rGO nanocomposite electrocatalysts coated on the Ni foam electrode in 1M KOH solution. Commercial Pt wire (99.9%) was used as a reference to compare with the as-synthesized catalysts for HER. The electrocatalytic performance of pure Ni foam was also studied to preclude the Ni-foam substrate role in the electrochemical reactions. Pt wire exhibits the small η_{10} indicating high catalytic activity. In Figure 3.6a, MoNi$_4$/MoO$_2$:rGO nanocomposite exhibits smaller η_{10} values indicating their catalytic activity is superior compared to Ni foam, MoNi$_4$/MoO$_2$ nanorod, and rGO catalysts (Table 3.1). This may be attributed to the graphene sheet providing a high surface area and accelerating the charge transfer to the electrode. Figure 3.6b summarized the η_{10} value of the as-synthesized electrocatalysts and the order of the η_{10} value is as follows: Ni foam (249 mV) > MoNi$_4$/MoO$_2$ nanorods (167 mV) > rGO (142 mV) >MoNi$_4$/MoO$_2$:rGO nanocomposite (122 mV), respectively. Figure 3.6c shows the corresponding Tafel slope of the as-synthesized catalysts, which was obtained from the LSV polarization curve. Generally, a small Tafel slope represents the fast reaction kinetics of the catalysts for HER. Tafel slopes are the intrinsic property of electrocatalysts which are calculated using the Tafel Equation (Equation 3.1):

$$\eta = b\ log\ J + a \qquad\qquad (3.1)$$

Where, η = overpotential, J = current density, b = Tafel slope, and a = intercept, respectively. As shown in Figure 3.6c, MoNi$_4$/MoO$_2$:rGO catalysts possesses the smallest Tafel slope (~53

mV dec^{-1}) compared with the Ni foam (~130 mV dec^{-1}), MoNi$_4$/MoO$_2$ (~82 mV dec^{-1}), and rGO (~64 mV dec^{-1}), indicating faster reaction kinetics and the HER processes are dominated by the Volmer- Heyrovsky reaction mechanism.

$$H_2O + e^- \rightarrow H_{ads} + OH^- \quad \text{(Volmer reaction)} \tag{3.2}$$

$$H_{ads} + H_2O + e^- \rightarrow H_2 \uparrow + OH^- \quad \text{(Heyrovsky reaction)} \tag{3.3}$$

$$H_{ads} + H_{ads} \rightarrow H_2 \quad \text{(Tafel reaction)} \tag{3.4}$$

HER kinetics at the electrode/electrolyte interface for as-synthesized MoNi$_4$/MoO$_2$, rGO, and MoNi$_4$/MoO$_2$:rGO electrocatalysts were investigated through electrochemical impedance spectroscopy (EIS) under the 1M KOH solution. The Randles circuit is used for fitting the EIS experimental results of MoNi$_4$/MoO$_2$, rGO, and MoNi$_4$/MoO$_2$:rGO as shown in the inset of Figure 3.6d, where R$_s$ is the solution resistance, R$_{ct}$ represents the charge transfer resistance, R$_p$ is the adsorption resistance, and CPE was corresponding to the constant phase elements. The corresponding values of R$_s$, R$_{ct}$, R$_p$, and CPE are listed in Table 3.1. As shown in Figure 3.6d, MoNi$_4$/MoO$_2$:rGO (2.10 Ω) exhibited a small charge transfer resistance compared with the MoNi$_4$/MoO$_2$ (4.20 Ω) and rGO (3.34 Ω), indicating an improved charge transfer rate (Figure 3.6e). It should be mainly due to the formation of conducting rGO layer and MoNi$_4$/MoO$_2$ that accelerates the charge transfer and reaction rate, improving its electrocatalytic hydrogen production performance. Apart from the electrochemical impedance spectroscopy (EIS), the long-term stability of MoNi$_4$/MoO$_2$:rGO nanocomposite was evaluated with the chronoamperometry (*j-t*) technique at a constant overpotential at 200 mV (vs. RHE) with a current density of 10 mA/cm^2 in 1M KOH solution. It is shown in Figure 3.6f that MoNi$_4$/MoO$_2$:rGO nanocomposite could maintain a steady current for over 12h without no detectable fade, exhibiting excellent stability in 1M KOH solution.

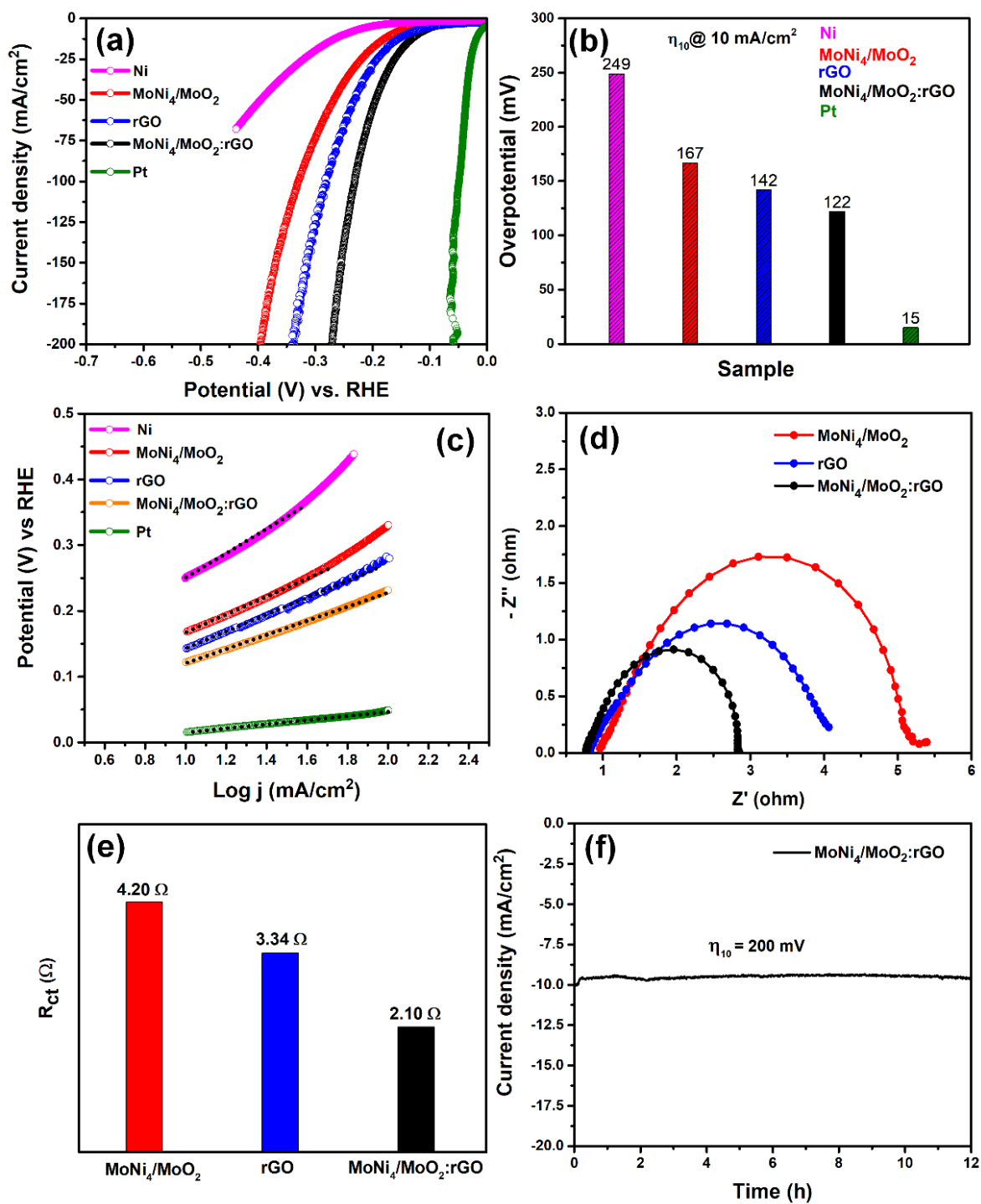***Figure* 3.6:** *(a) Polarization curve for HER on Ni foam (1×1cm^2) area; (b) corresponding overpotential (η$_{10}$); (c) Tafel plots for the various catalysts derived from the LSV; (d) EIS Nyquist plot; (e) corresponding charge transfer resistance (R$_{ct}$), and (f) Chronoamperometric (j-t) response for MoNi$_4$/MoO$_2$:rGO nanocomposite at a constant overpotential of 200 mV.*

Table 3.1: Lists the electrochemical parameters of various electrocatalysts samples of $MoNi_4/MoO_2$, rGO, and $MoNi_4/MoO_2$:rGO nanocomposite.

Sample name	η (mV) at 10 mA/cm^2	β (mV dec^{-1})	R_s (Ω)	R_{ct} (Ω)	R_p (Ω)	CPE_1 (S-sec^n)	CPE_2 (S-sec^n)
Ni foam	249	130	-	-	-	-	-
$MoNi_4/MoO_2$	167	82	0.98	4.20	0.75	0.0004	0.0005
rGO	142	64	0.84	3.34	0.43	0.0001	0.0023
$MoNi_4/MoO_2$:rGO	122	53	0.77	2.10	0.57	0.0004	0.0005
Pt	15	34	-	-	-	-	-

Overall, in the $MoNi_4/MoO_2$:rGO nanocomposite material, we obtained the simultaneous effects of both $MoNi_4/MoO_2$ and rGO while properties of both the materials play an important role in enhancing the catalytic activities of the composite. In the composite structure both the signature of $MoNi_4/MoO_2$ and rGO were obtained as discussed in XRD and Raman analysis. Owing to the in-situ synthesis of the composite material, it seems chemically derived interface was formed, which helps binding both the components together as discussed in the TEM section. Finally, the nanocomposite materials showed enhanced HER performance compared to both its components, which manifests the simultaneous electrocatalytic effects of both $MoNi_4/MoO_2$ and rGO. Specifically, $MoNi_4/MoO_2$ contributes towards water electrolysis via Volmer-Heyrovsky mechanisms and promotes the faster adsorption and desorption of H_3O^+ in aqueous medium. On the other hand, rGO typically act as a conducting channel for the electron transport and imparts the stability of the HER electrodes. Since the rGO retain a defective structure with various functional molecules and

localized carbon vacancies [41], it exhibits localized electron concentrations that also play a significant effect in water electrolysis. In addition, the edge-plane like structures of rGO takes part in the catalytically active charge transfer at the interface, which simultaneously accelerates the charge-transfer kinetics at the electrode/electrolyte interface [19]. Thus, apart from conducting pathways, rGO in the nanocomposite significantly enhance the electrocatalysis along with $MoNi_4/MoO_2$, which together improve the HER performance of the nanocomposite electrodes. We believe that such type of work will opens up numerous possibilities of developing noble-metal-free high-performance hierarchical nanocomposites comprises of 2D-nanostructures and nano-scale electrocatalysts for improving the HER performance via water electrolysis.

3.3 Chapter summary

In summary, the graphene layer supported $MoNi_4/MoO_2$ nanorods were synthesized by using one-pot hydrothermal process followed by annealing at 500 ℃. The nanocomposite exhibits the presence of both the $MoNi_4/MoO_2$ and rGO structures intact as designated via XRD, Raman and TEM/SAED data. The as-synthesized $MoNi_4/MoO_2$:rGO nanocomposites shows the active catalytic performance for hydrogen evaluation reaction (HER), as well as stable durability for 12 h in 1M KOH solution. The electrocatalytic HER performance of nanocomposite supersedes the efficacy of both the $MoNi_4/MoO_2$ and rGO, while graphene support provides a high surface area, conducting pathways for the electron transfer. Also, the edge-plane like structure of catalytically active sites and localized surface defects of rGO contributes towards improving the performance of the overall HER efficiency of the nanocomposite, thereby, accelerates the charge transfer and lowering the diffusion coefficient for accelerating the charge-transfer kinetics. In general, this work fundamentally highlights the advancement on developing noble-metal-free electrocatalytic materials for hydrogen evaluation reaction (HER).

References

[1]   X. Sun *et al.*, "Semimetallic molybdenum disulfide ultrathin nanosheets as an efficient electrocatalyst for hydrogen evolution," *Nanoscale,* vol. 6, no. 14, pp. 8359-8367, 2014, doi: 10.1039/C4NR01894J.

[2]   Y. Yin *et al.*, "Synergistic Phase and Disorder Engineering in 1T-MoSe$_2$ Nanosheets for Enhanced Hydrogen-Evolution Reaction," *Advanced Materials,* vol. 29, no. 28, p. 1700311, 2017, doi: https://doi.org/10.1002/adma.201700311.

[3]   M. A. Lukowski *et al.*, "Highly active hydrogen evolution catalysis from metallic WS$_2$ nanosheets," *Energy & Environmental Science,* vol. 7, no. 8, pp. 2608-2613, 2014, doi: 10.1039/C4EE01329H.

[4]   B. Hinnemann *et al.*, "Biomimetic Hydrogen Evolution: MoS2 Nanoparticles as Catalyst for Hydrogen Evolution," *Journal of the American Chemical Society,* vol. 127, no. 15, pp. 5308-5309, 2005, doi: 10.1021/ja0504690.

[5]   B. Albert and H. Hillebrecht, "Boron: Elementary Challenge for Experimenters and Theoreticians," *Angewandte Chemie International Edition,* vol. 48, no. 46, pp. 8640-8668, 2009, doi: https://doi.org/10.1002/anie.200903246.

[6]   S. Gupta, N. Patel, A. Miotello, and D. C. Kothari, "Cobalt-Boride: An efficient and robust electrocatalyst for Hydrogen Evolution Reaction," *Journal of Power Sources,* vol. 279, pp. 620-625, 2015, doi: https://doi.org/10.1016/j.jpowsour.2015.01.009.

[7]   H. Yan *et al.*, "Phosphorus-Modified Tungsten Nitride/Reduced Graphene Oxide as a High-Performance, Non-Noble-Metal Electrocatalyst for the Hydrogen Evolution Reaction," *Angewandte Chemie International Edition,* vol. 54, no. 21, pp. 6325-6329, 2015, doi: https://doi.org/10.1002/anie.201501419.

[8]   H. B. Wu, B. Y. Xia, L. Yu, X.-Y. Yu, and X. W. Lou, "Porous molybdenum carbide nano-octahedrons synthesized via confined carburization in metal-organic frameworks for efficient hydrogen production," *Nature Communications,* vol. 6, no. 1, p. 6512, 2015, doi: 10.1038/ncomms7512.

[9]   C. Tang *et al.*, "Fe-Doped CoP Nanoarray: A Monolithic Multifunctional Catalyst for Highly Efficient Hydrogen Generation," *Advanced Materials,* vol. 29, no. 2, p. 1602441, 2017, doi: https://doi.org/10.1002/adma.201602441.

[10]   Y.-Y. Chen *et al.*, "Self-Templated Fabrication of MoNi$_4$/MoO$_{3-x}$ Nanorod Arrays with Dual Active Components for Highly Efficient Hydrogen Evolution," *Advanced Materials,* vol. 29, no. 39, p. 1703311, 2017, doi: https://doi.org/10.1002/adma.201703311.

[11]   J. Zhang *et al.*, "Efficient hydrogen production on MoNi$_4$ electrocatalysts with fast water dissociation kinetics," *Nature Communications,* vol. 8, no. 1, p. 15437, 2017, doi: 10.1038/ncomms15437.

[12]   J. Deng, P. Ren, D. Deng, L. Yu, F. Yang, and X. Bao, "Highly active and durable non-precious-metal catalysts encapsulated in carbon nanotubes for hydrogen evolution reaction," *Energy & Environmental Science,* vol. 7, no. 6, pp. 1919-1923, 2014, doi: 10.1039/C4EE00370E.

[13]   Y. Zhao *et al.*, "Defect-Engineered Ultrathin δ-MnO2 Nanosheet Arrays as Bifunctional Electrodes for Efficient Overall Water Splitting," *Advanced Energy Materials,* vol. 7, no. 18, p. 1700005, 2017, doi: https://doi.org/10.1002/aenm.201700005.

[14]   U. Sharma, S. Karazhanov, R. Jose, and S. Das, "Plasmonic hot-electron assisted phase transformation in 2D-MoS$_2$ for the hydrogen evolution reaction: current status and future prospects," *Journal of Materials Chemistry A,* vol. 10, no. 16, pp. 8626-8655, 2022, doi: 10.1039/D1TA10918A.

[15]   U. Sharma, S. Karazhanov, N. Alonso-Vante, and S. Das, "Metallic-phase of MoS$_2$ as potential electrocatalyst for hydrogen production via water splitting: A brief review," *Current Opinion in Electrochemistry,* vol. 35, p. 101067, 2022.

[16]   X. Fan, Z. Peng, J. Wang, R. Ye, H. Zhou, and X. Guo, "Carbon-Based Composite as an Efficient and Stable Metal-Free Electrocatalyst," *Advanced Functional Materials,* vol. 26, no. 21, pp. 3621-3629, 2016, doi: https://doi.org/10.1002/adfm.201600076.

[17]   Y. Zheng *et al.*, "Hydrogen evolution by a metal-free electrocatalyst," *Nature Communications,* vol. 5, no. 1, p. 3783, 2014, doi: 10.1038/ncomms4783.

[18]   V. K. Singh, U. Gupta, B. Mukherjee, S. Chattopadhyay, and S. Das, "MoS$_2$ Nanosheets on MoNi$_4$/MoO$_2$ Nanorods for Hydrogen Evolution," *ACS Applied Nano Materials,* vol. 4, no. 1, pp. 886-896, 2021, doi: 10.1021/acsanm.0c03296.

[19]   L. An, X. Zang, L. Ma, J. Guo, Q. Liu, and X. Zhang, "Graphene layer encapsulated MoNi$_4$-NiMoO$_4$ for electrocatalytic water splitting," *Applied Surface Science,* vol. 504, p. 144390, 2020, doi: https://doi.org/10.1016/j.apsusc.2019.144390.

[20]   P. D. Tran *et al.*, "Coordination polymer structure and revisited hydrogen evolution catalytic mechanism for amorphous molybdenum sulfide," *Nature Materials,* vol. 15, no. 6, pp. 640-646, 2016, doi: 10.1038/nmat4588.

[21]   J. W. D. Ng *et al.*, "Gold-supported cerium-doped NiO$_x$ catalysts for water oxidation," *Nature Energy,* vol. 1, no. 5, p. 16053, 2016, doi: 10.1038/nenergy.2016.53.

[22]   Y. Zhou *et al.*, "Topological Formation of a Mo–Ni-Based Hollow Structure as a Highly Efficient Electrocatalyst for the Hydrogen Evolution Reaction in Alkaline Solutions," *ACS Applied Materials & Interfaces,* vol. 11, no. 24, pp. 21998-22004, 2019, doi: 10.1021/acsami.9b03686.

[23]   Y. B. Tan and J.-M. Lee, "Graphene for supercapacitor applications," *Journal of Materials Chemistry A,* vol. 1, no. 47, pp. 14814-14843, 2013, doi: 10.1039/C3TA12193C.

[24]   J. Zhu, R. Duan, S. Zhang, N. Jiang, Y. Zhang, and J. Zhu, "The application of graphene in lithium ion battery electrode materials," *SpringerPlus,* vol. 3, no. 1, p. 585, 2014, doi: 10.1186/2193-1801-3-585.

[25]   X. Kong *et al.*, "Graphene/Si Schottky solar cells: a review of recent advances and prospects," *RSC Advances,* vol. 9, no. 2, pp. 863-877, 2019, doi: 10.1039/C8RA08035F.

[26]   Y. Yan *et al.*, "A recent trend: application of graphene in catalysis," *Carbon Letters,* vol. 31, no. 2, pp. 177-199, 2021, doi: 10.1007/s42823-020-00200-7.

[27]   J. Wang, X. Mu, M. Sun, and T. Mu, "Optoelectronic properties and applications of graphene-based hybrid nanomaterials and van der Waals heterostructures," *Applied Materials Today,* vol. 16, pp. 1-20, 2019, doi: https://doi.org/10.1016/j.apmt.2019.03.006.

[28]   K.-Q. Lu, Y.-H. Li, Z.-R. Tang, and Y.-J. Xu, "Roles of Graphene Oxide in Heterogeneous Photocatalysis," *ACS Materials Au,* vol. 1, no. 1, pp. 37-54, 2021, doi: 10.1021/acsmaterialsau.1c00022.

[29]   D. Biplab Kumar Kuila and Shaikh Mohammed Zaeem and Soumili Daripa and Kanak Kaushik and Saral Kumar Gupta and Santanu, "Mesoporous Mn $_3$O$_4$ coated reduced graphene oxide for high-performance supercapacitor applications," *Materials Research Express,* vol. 6, no. 1, p. 015037, 2019.

[30]   R. Bhattacharyya *et al.*, "Graphene oxide-ferrite hybrid framework as enhanced broadband absorption in gigahertz frequencies," *Scientific Reports,* vol. 9, no. 1, p. 12111, 2019, doi: 10.1038/s41598-019-48487-5.

[31]   G. Jiménez-Martín *et al.*, "Graphene-based Activated Carbon Composites for High Performance Lithium-Sulfur Batteries," *Batteries & Supercaps,* vol. n/a, no. n/a, p. e202200167, doi: https://doi.org/10.1002/batt.202200167.

[32]   P. Solís-Fernández, M. Bissett, and H. Ago, "Synthesis, structure and applications of graphene-based 2D heterostructures," *Chemical Society Reviews,* vol. 46, no. 15, pp. 4572-4613, 2017, doi: 10.1039/C7CS00160F.

[33]   A. R. Marlinda, N. Yusoff, S. Sagadevan, and M. R. Johan, "Recent developments in reduced graphene oxide nanocomposites for photoelectrochemical water-splitting applications," *International Journal of Hydrogen Energy,* vol. 45, no. 21, pp. 11976-11994, 2020, doi: https://doi.org/10.1016/j.ijhydene.2020.02.096.

[34]   T.-F. Yeh, J. Cihlář, C.-Y. Chang, C. Cheng, and H. Teng, "Roles of graphene oxide in photocatalytic water splitting," *Materials Today,* vol. 16, no. 3, pp. 78-84, 2013, doi: https://doi.org/10.1016/j.mattod.2013.03.006.

[35]   S. Chakrabarty, A. Mukherjee, and S. Basu, "RGO-MoS$_2$ Supported NiCo$_2$O$_4$ Catalyst toward Solar Water Splitting and Dye Degradation," *ACS Sustainable Chemistry & Engineering,* vol. 6, no. 4, pp. 5238-5247, 2018, doi: 10.1021/acssuschemeng.7b04757.

[36]   S. J. Gutić, A. S. Dobrota, M. Leetmaa, N. V. Skorodumova, S. V. Mentus, and I. A. Pašti, "Improved catalysts for hydrogen evolution reaction in alkaline solutions through the

electrochemical formation of nickel-reduced graphene oxide interface," *Physical Chemistry Chemical Physics,* vol. 19, no. 20, pp. 13281-13293, 2017, doi: 10.1039/C7CP01237C.

[37]   J. Ahmed *et al.*, "rGO supported $NiWO_4$ nanocomposites for hydrogen evolution reactions," *Materials Letters,* vol. 240, pp. 51-54, 2019, doi: https://doi.org/10.1016/j.matlet.2018.12.114.

[38]   X. Wang *et al.*, "Defect in reduced graphene oxide tailored selectivity of photocatalytic CO_2 reduction on Cs_4PbBr_6 pervoskite hole-in-microdisk structure," *Nano Energy,* vol. 78, p. 105388, 2020, doi: https://doi.org/10.1016/j.nanoen.2020.105388.

[39]   C. Liu, H. Yan, Z. Chen, L. Yuan, and Q. Lv, "Effect of surface-functionalized reduced graphene oxide on mechanical and tribological properties of bismaleimide composites," *RSC Advances,* vol. 5, no. 58, pp. 46632-46639, 2015, doi: 10.1039/C5RA06009E.

[40]   S. Georgitsopoulou, O. Petrai, and V. Georgakilas, "Highly conductive functionalized reduced graphene oxide," *Surfaces and Interfaces,* vol. 16, pp. 152-156, 2019, doi: https://doi.org/10.1016/j.surfin.2019.05.010.

[41]   R. Bhattacharyya, V. Kumar Singh, S. Bhattacharyya, P. Maiti, and S. Das, "Defect reconstructions in graphene for excellent broadband absorption properties with enhanced bandwidth," *Applied Surface Science,* vol. 537, p. 147840, 2021, doi: https://doi.org/10.1016/j.apsusc.2020.147840.

[42]   P. K. Narayanam, P. Soni, V. D. Botcha, G. Singh, and S. S. Major, "Transparent and Hydrophobic "Reduced Graphene Oxide–Titanium Dioxide" Nanocomposites for Nonwetting Device Applications," *ACS Applied Nano Materials,* vol. 1, no. 10, pp. 5691-5701, 2018, doi: 10.1021/acsanm.8b01302.

[43]   H. Kolya and C.-W. Kang, "Polyvinyl acetate/reduced graphene oxide-poly (diallyl dimethylammonium chloride) composite coated wood surface reveals improved hydrophobicity," *Progress in Organic Coatings,* vol. 156, p. 106253, 2021, doi: https://doi.org/10.1016/j.porgcoat.2021.106253.